RSC Advances

PAPER

View Article Online
View Journal | View Issue

Cite this: *RSC Adv.*, 2020, **10**, 22440

Towards 3D-lithium ion microbatteries based on silicon/graphite blend anodes using a dispenser printing technique†

Mathias Drews,[a] Sebastian Tepner,[a] Peter Haberzettl,[a] Harald Gentischer,[a] Witali Beichel,[a] Matthias Breitwieser,[bc] Severin Vierrath[b] and Daniel Biro*[a]

Received 8th April 2020
Accepted 27th May 2020

DOI: 10.1039/d0ra03161e

rsc.li/rsc-advances

In this work we present for the first time high capacity silicon/carbon–graphite blend slurries designed for application in 3D-printed lithium ion microbatteries (3D-MLIBs). The correlation between electrochemical and rheological properties of the corresponding slurries was systematically investigated with the prospect of production by an automated dispensing process. A variation of the binder content (carboxymethyl cellulose/styrene–butadiene rubber, CMC/SBR) between 6 wt%, 12 wt%, 18 wt% and 24 wt% in the anode slurry proved to be crucial for the printing process. Regarding the rheological properties increasing binder content leads to increased viscosity and yield stress values promising printed structures with high aspect ratios. Consequently, interdigital 3D-printed micro anode structures with increasing aspect ratios were printed with increasing binder content. For printed 6-layer structures aspect ratios of 6.5 were achieved with anode slurries containing 24 wt% binder. Electrochemical results from planar coin cell measurements showed that anodes containing 12 wt% CMC/SBR binder content exhibited stable cycling at the highest charge capacities of 484 mA h g^{-1} at a current rate of C/4. Furthermore, at 4C the cells showed high capacity retention of 89% compared to cycling at C/4. Based on this study and the given material formulation we recommend 18 wt% CMC/SBR as the best trade-off between electrochemical and rheological properties for future work with fully 3D-printed MLIBs.

Introduction

The increasing market of small electronic devices in the field of the internet of things (IOT) such as wearables, smart electronics and medical implants requires suitable energy storage devices. Lithium ion batteries (LIB) are currently the batteries of choice for microelectronics, due to their high gravimetric (W h kg^{-1}) and volumetric energies (W h l^{-1}).[1] However, conventionally designed LIBs (*i.e.* pouch, prismatic, cylindrical) are difficult to miniaturize. On the other hand supercapacitors and thin film batteries can be miniaturized and are already used in microelectronic devices, but at the expense of energy density.[2–5] For thin film batteries energy and power density can be increased by achieving 3D-structured cathodes.[6,7] Additive manufactured microbatteries are a promising technology that can handle the integration problem into electronic devices and have the potential to reach high power at high energy density levels simultaneously. To achieve this, the principle idea of 3D-manufactured batteries is to decouple ionic and electronic transport processes. In the additive manufacturing process active material is deposited in the *z*-direction of the current collector which leads to tall and preferable small 3D-battery structures. Such high aspect ratio (AR) electrodes are considered to have the advantage of increased energy per footprint area whereas the electrode thickness and therefore the ionic pathway is kept constant. Thus, energy density can be increased by a steady value of power density where the major rate limiting factor is the electric resistance of the electrodes.[8] In conventional planar electrode batteries either power or energy density can be optimized by adjusting the electrode thickness.[9] The basic idea of 3D-printed microbatteries is illustrated in Fig. 1.

There are several different ways to manufacture 3D-battery structures *e.g.* by using electrodeposition,[10,11] inkjet[12,13] and dispenser printing techniques.[8,14–16] Additive manufacturing based on dispenser printing represents a simple and low cost microbattery production process.[17] Furthermore, slurry formulation can be adopted from industrial battery cell production by adjusting the amount or type of specific components. Fu *et al.* presented an interdigitated lithium ion microbattery (IMLIB) based on lithium iron phosphate/graphene oxide (LFP/GO) cathodes and lithium-titanate/graphene oxide (LTO/GO)

[a]*Fraunhofer Institute for Solar Energy Systems ISE, Heidenhofstraße 2, 79110 Freiburg im Breisgau, Germany. E-mail: daniel.biro@ise.fraunhofer.de; Tel: +49-761-4588-5246*

[b]*Electrochemical Energy Systems, IMTEK – Department of Microsystems Engineering, University of Freiburg, Georges-Koehler-Allee 103, 79110 Freiburg im Breisgau, Germany*

[c]*Hahn-Schickard, Georges-Koehler-Allee 103, 79110 Freiburg im Breisgau, Germany*

† Electronic supplementary information (ESI) available. See DOI: 10.1039/d0ra03161e

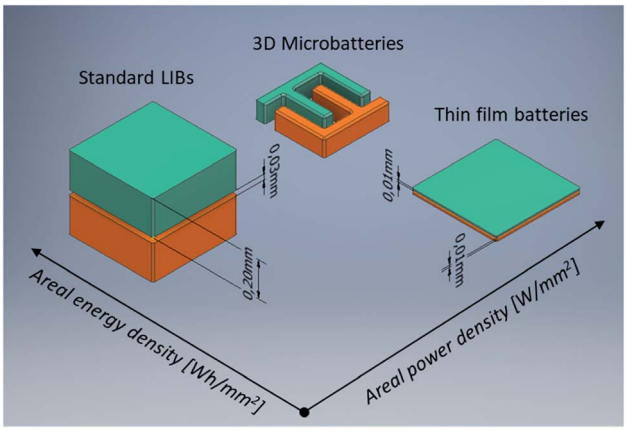

Fig. 1 Principle idea of energy and power optimization in 3D-printed batteries. The shown dimensions give the scale of the electrode thickness rather than an accurate value.

anodes with 10 wt% of PVDF binder. The printed full cell with a size of 7 × 3 mm^2 showed limited cycling behavior <20 cycles with a capacity of 100 mA h g^{-1} at a current rate of 50 mA g^{-1}.[15] So far, the smallest printed 3D-battery structures using the dispenser printing approach were published by Sun *et al.* in 2013.[8] The cell consisting of an LTO anode and LFP cathode and had dimensions of approximately 1 × 1 mm^2 (5 anode and cathode fingers) at a height of approx. 190 μm. Wei *et al.* manufactured biphasic electrodes for customized planar lithium ion batteries with electrode thicknesses up to 1 mm. Areal energy density could be increased by more than one order of magnitude at constant areal power densities compared to electrodes with 0.05 mm thickness.[14] With respect to slurry development for 3D-printed batteries Li *et al.* showed that the detailed investigation of electrochemistry and slurry rheology is crucial for a successful production of additive manufactured microbatteries.[18] However, in the field of suspension rheology and its impact on printability by the dispensing method Pospischil *et al.* demonstrated that there are more rheological parameters (*e.g.* yield stress), which need to be investigated, especially, when high aspect ratio dispensing is desired.[19] Furthermore, in another work the same authors showed that aspect ratios of dispensed structures are strongly influenced by the underlying surface properties and process parameters for a variety of different photovoltaics applications.[20]

Based on experiences from photovoltaic applications, we investigate in this study customized Si/C–graphite blend slurries as anode for 3D-MLIBs unprecedented in scientific reports. As it was already stated earlier in this manuscript energy density of 3D-printed batteries can be increased by depositing active material in the *z*-direction whereas power density of the cell remains constant. In addition to this fundamental property of additive manufactured batteries we have chosen high capacity Si/C–graphite blend anodes to increase the energy density of the cell not only from a geometrical but also a material perspective. The investigation of the corresponding slurries includes a systematic investigation of the correlation between slurry rheology and electrochemical battery characteristics. Rheological investigations are key to adjust dispenser printing properties regarding the quality of printed structures. The amount of binder was considered a crucial factor influencing the electrochemical and rheological properties. Consequently, Si/C–graphite blend anode slurries were prepared with varying amounts of binder and investigated regarding the electrochemical rate performance, rheological behavior and the quality of the printed interdigitated structures.

Experimental

Materials and slurry preparation

For the preparation of Si/C (made from crystalline silicon nanoparticles APS ≈ 100 nm, 99%, plasma synthesized, Alfa Aesar)–graphite blend anode slurries carboxymethyl cellulose (CMC, Merck group) was suspended in deionized water by magnetic stirring for 6 h. When the dispersion was fully homogenized the styrene–butadiene rubber (SBR) dispersion (85 wt% water, Targray group) was added. The ratio between CMC and SBR was 50/50 (wt%/wt%) and slurries with a binder content of 6, 12, 18 and 24 wt% were investigated. A binder content of 6 wt% was chosen since this value is close to planar industry-orientated Si/C–graphite blend anodes. However, binder contents of lower than 6 wt% were found to have relatively low viscosities and were thus suggested to be scarcely relevant for 3D-printing processes. In pretests, slurries with binder a content of 24 wt% were found to be difficult to process by laboratory equipment such as magnetic stirrers whereby a homogenization of the slurry *via* magnetic stirring could not necessarily be ensured. After another 30 min of stirring the Si/C, graphite (APS 7 – 11 μm Alfa Aesar, 99%) and carbon black (Alfa Aesar, 100% compressed, 99.9%) were added. The amount of silicon in the blended material was aimed to be 12 wt%. For a detailed overview of the composition of each slurry see Table 1. Here solid fractions are listed for dispenser printing experiment. For rheological measurements values are given only for slurries with the highest solid content (aimed to be 40 wt%). In the ensuing sections the term "40 wt%" acts as an abbreviation for these numbers. Corresponding values for slurries with lower solid content can be found in the section regarding rheological characterization. For electrochemical measurements solid contents of 40 wt% were desired but not specifically measured. All components were mixed (DAC 150/250, Speedmixer, Germany) at 3500 rpm for 2 min (2 times with 10 min rest). A three roll mill (80E, Exakt Advanced Technologies, Germany) with a large roll distance of 10 μm and a small roll distance of 5 μm was used to adjust the particle size of the components and to homogenize the slurry. The process time in the three roll mill was minimized (60–90 s) to have as less water evaporation as possible. For the determination of the solid fraction three samples were taken from the three roll mill and weighed before and after drying. For rheology and dispenser printing the slurries were used immediately. For anode preparation the slurries were coated on copper foil *via* doctor blade technique with a wet film thickness of 50 μm and dried at 313.15 K overnight. After predrying 14 mm coins were punched out and dried under vacuum at 393.15 K overnight.

Table 1 Composition of Si/C–graphite blend slurries

						Solid fraction [wt%]
Binder content	Si/C [wt%]	Graphite [wt%]	Carbon black [wt%]	CMC [wt%]	SBR [wt%]	Rheology/dispensing
6 wt%	18.8	69.5	5.7	3.0	3.0	42.5/41.7
12 wt%	17.6	65.0	5.4	6.0	6.0	42.6/42.3
18 wt%	16.4	60.6	5.0	9.0	9.0	44.1/43.4
24 wt%	15.2	56.2	4.6	12.0	12.0	43.1/43.8

Physiochemical characterization

BET surface measurements of the Si/C material were performed on a QuadraSorb Station 3 (Quantachrome Instruments) instrument. Raman measurements were conducted on an Alpha500 (WITec, Germany) confocal Raman microscope with a laser wavelength of 532 nm. X-ray diffraction patterns were collected using a Miniflex 600 (Rigaku, Japan) with a copper source ($\lambda = 1.54$ Å), a stepwidth of 0.02° and speed of 0.1° min^{-1} operating at 40 kV and 15 mA. For particle size distribution measurements an LS 13 320 Laser Diffraction Particle Size Analyzer from Beckman Coulter was used.[21,22] The samples were mixed thoroughly as aqueous colloid suspensions containing tensides to prevent the formation of aggregates. The colloid suspensions were dispersed by an ultrasonic lance before measurement (5 times for 60 s each).

Rheological characterization

For rheological measurements a commercial rotational rheometer (Anton Paar, Germany) was used. Two types of measurements were conducted to determine the shear rate dependent viscosity and the yield stress for each slurry. A measurement protocol according to Tepner *et al.* was used in this study.[23,24] For both measurements, a plate–plate geometry was chosen. The upper plate had a surface roughness of 2–4 μm and was 25 mm in diameter at a measurement gap of 500 μm. All slurries were investigated regarding their shear viscosity. For this a successive shear controlled measurement protocol from 0.1 s^{-1} to 200 s^{-1} was chosen with 40 points per decade. Prior to the measurement, the edge of the rotating plate was cleared of excess slurry as described in literature.[23] To investigate the yield stress of all slurries the procedure was similar with the exception that the measurement was shear stress controlled in the range from 1 to 10 000 Pa with 40 points per decade. Finally the critical yield stress was determined using the tangent intersection method.[25] The mean values of three measurements are presented. All measurements were done at 25 °C. To avoid preshearing each measurement was done with a new batch of slurry.

3D-Dispenser printing and subsequent analysis of the structure

The dispensing experiments for the 3D-microbatteries were conducted on a commercially available table robot (VR3303, Vieweg, Germany). The robot allows for a precise relative movement between the dispensing nozzle and the substrate in 3 dimensions with an accuracy of 8 μm in the *x*,*y*-direction and 1 μm in the *z*-direction. Each structure was printed on a copper substrate. Before processing the copper was cleaned in an 18% HCl solution. The offset between substrate and nozzle was set to 240 μm and the step size in the *z*-direction (rise of the nozzle after each printed layer) was set to 140 μm. Depending on the rheological parameters of each slurry, it was necessary to evaluate the correct pressure in order to ensure a sufficient volume flow rate for a given speed ($v_{x,y}$) of the table robot.[26,27] Here the pressure was set to 1.2, 1.6, 2.0 and 3.2 bar for the sample with 6 wt%, 12 wt%, 18 wt% and 24 wt% binder, respectively. The diameter of the micro nozzle (Vieweg, Germany) was 110 μm. Fig. 2 shows a simple sketch of a section of an interdigitated battery structure including dimensioning (defining anode and cathode does not play an important role in this case). As it was already discussed high aspect ratios increase the energy density per footprint area. Thus, high ARs were desired by dispensing 8 layers on top of each other and the development of the AR was investigated at 2-, 4-, 6- and 8-layered structures.

3D-printed anode structures were dried for 24 h at ambient conditions. A scanning electron microscope (Auriga 60, Zeiss, Germany) was used at an acceleration voltage of 7.0 kV to image the microstructure of the samples. A confocal laser microscope (Lext Series, Olympus) was employed to measure the mean average height and the mean average width of the dispensed structures. The capacity per footprint area was calculated using the mass of the anode considering the active fraction and the base area of the structure. Regarding the latter the finger width was taken from microscopy analysis whereas finger lengths

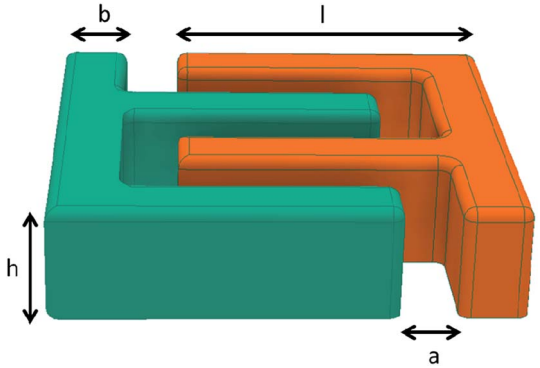

Fig. 2 Sketch of a section of an interdigitated (battery) structure.

were not directly measured but rather taken from the path-length the dispensing robot travelled.

Electrochemical characterization

Half cells were assembled in an argon filled glovebox (E-Line, GS Glovebox System, Germany, O_2 < 3 ppm, H_2O < 0.5 ppm) in CR2032 coin cells using Si/C–graphite blend electrodes, lithium metal as counter electrode, 1 mm glass fibre separator (EL-Cell, Germany) soaked with 150 μl LP30 (1 M $LiPF_6$ in ethylene carbonate (EC)/dimethyl carbonate (DMC) 50/50 (v%/v%)) + 10 wt% (fluoroethylene carbonate) FEC (Merck group) as electrolyte. Rate capability tests were performed on a BCS-805 (BioLogic, France) battery tester in the voltage range between 1.5 V and 0.01 V in CC setup with a CV step at the lower cut-off voltage and 10 min rest after each lithiation step. Formation cycles included two cycles at C/10 and two cycles at C/5. Cells were cycled at C/4, C/2, 1C, 2C and 4C each for 10 cycles.

Results and discussion

Material composition of Si/C slurries

The Si/C–graphite blend materials were characterized by Raman spectroscopy, X-ray diffraction and nitrogen physisorption experiments (BET surface). While bulk silicon shows a Raman mode at 521 cm^{-1}, the corresponding mode of the Si/C sample used in this study has a signal at 515 cm^{-1}. This shift is commonly known and due to the silicon particle size. Silicon nanoparticles show a shift to lower wavenumbers compared to the signal of bulk silicon.[28,29] The carbon related D- and G-band is shown at 1350 cm^{-1} and 1585 cm^{-1}, respectively[30,31] (see Fig. S1†). The ratio between the area of the D- and G-band (A(D)/A(G)) is calculated as 2.5 ± 0.6 which suggests a relatively high amount of disordered carbon in the Si/C anode material. In the XRD spectrum all silicon- and carbon-related peaks could be assigned to the corresponding reflection planes (see Fig. S2†). The BET surface area of the Si/C particles was determined to be 14.1 m^2 g^{-1}, which is in good accordance with literature values.[32,33]

Particle size distribution

Particle size has a major impact on both, the electrochemical properties and the printing processes. Si/C particles were ball milled in order to adjust particle size with respect to electrochemical and dispenser printing optimization. It is commonly known that smaller particle sizes promote electrochemical performance.[34,35] Regarding dispensing processes particles need to reach sufficiently small sizes to prevent clogging of the nozzle.[19] The latter is extremely important for industrial processes, where the breakdown of machines and significant downtime is unacceptable in terms of production cost. However, Si/C particles should not be milled too small to maintain a homogeneous composite material and prevent fresh silicon surface formation. The latter would be detrimental for battery cell performance. Particle size distributions of the Si/C composite material after ball milling and exemplary of a Si/C–graphite slurry with 18 wt% binder (only values of slurry with 18 wt% binder are shown since this slurry will be recommended for fully printed 3D-MLIBs) are given in the ESI.† D_{10} and D_{90} values of the Si/C composite are evaluated to 2.1 ± 0.2 μm and 43.5 ± 0.3 μm, respectively. Corresponding values for the slurry are 1.9 ± 0.2 μm and 17.4 ± 0.3 μm. The D_{90} values of the slurry are significantly smaller compared to the pure composite which refers to the impact of the three roll mill on the slurry production. Since the Si/C composite are suggested to represent the biggest particles in the slurry, changes in characteristics of the particle size distribution are mostly attributed to the crushing of the Si/C particles. It needs to be mentioned that the three roll mill process is absolute necessary, since only after this additional treatment the corresponding slurries become extractable through a 110 μm nozzle.

Rheological properties of Si/C slurries

Rheological investigation is a powerful instrument and essential to characterize slurries with respect to dispenser printing processes. Viscosity and yield stress values are significant quantities for prediction of high AR structures and can be measured to estimate slurry behavior in micro nozzle openings. In Fig. 3a, the shear rate dependent viscosity for the different types of slurries is presented, revealing a strong non Newtonian flow behavior. Especially at low shear rates (10^{-1} to 10^{0} s^{-1}), the viscosity increases with the amount of binder in the sample. Regarding dispenser printing processes it was shown that slurries should have significantly increased viscosities compared to slurries from standard coating processes and are in the range of 10^3 to 10^4 Pa at 1 s^{-1}.[8,14,15] Thus the binder content should be increased to guarantee a high viscosity after nozzle exit when thixotropic effects are neglected.[19] During the dispensing process the shear rate in the micro nozzle correlates linearly with the process speed. For industrial dispenser process speeds the shear rate is surpassing 5000 s^{-1}, which cannot be measured with commercial rotational rheometers due to significant sample spillage at high rotation speeds.[23,36] Here all paste samples show similar viscosities at high shear rates (see Fig. 3a) but differ significantly during dispensing experiments in terms of their printed line geometry. Thus the shear rate dependent viscosity is not the dominant factor when it comes to high speed dispensing through nozzle openings in the micrometer range. Pospischil *et al.* showed that the shape of the printed structure strongly correlates with the yield stress of the slurry, which describes the necessary shear stress where the slurry transitions from elastic- to plastic-deformation.[19] Therefore, yield stress measurements are crucial for dispenser printing processes and presented in Fig. 3b. At a given shear stress, the rate of deformation changes from linear towards an exponential rate of increase. The intersection point defines the yield stress and is calculated by the tangent intersection method.[25] In Fig. 3c, measurements of the yield stress for all corresponding combinations of the solid and the binder content are shown. The yield stress increases with increasing solid and binder content. A combination of both is quite promising to generate tall AR structures. However, increasing the solid content in the paste is limited because a sufficient

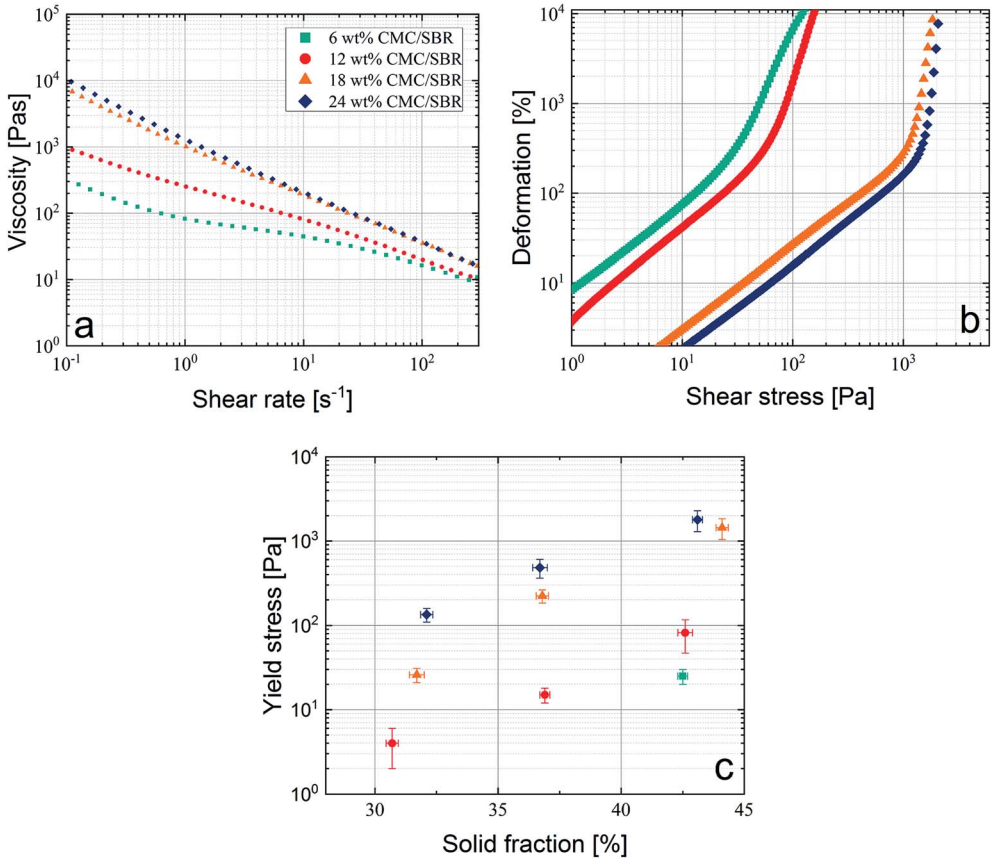

Fig. 3 (a) Shear viscosity for four slurries with different binder contents as a function of the shear rate and (b) corresponding yield stress measurements. (c) Yield stress values, calculated by the tangent intersection method, are presented in dependence of the binder content and the solid fraction.[25] Legend is the same for (a)–(c).

printability requires a certain content of the binder/solvent mixture which dictates the shear thinning nature of the paste and therefore the paste flow within the micro nozzle. To reach preferably high yield stresses for the dispenser printing experiments, only slurries with 40 wt% solid content were used. For lower solid contents of the sample with 6 wt% binder the measurement procedure of the yield stress does not create sufficient results because the yield stress value is too low. Thus, it is hardly possible to measure the elastic behavior of the sample, which fulfills Hooke's Law in a reproducible manner. Therefore, yield stress values for the 6 wt% binder sample with a solid content below 40 wt% are not presented.

Dispenser printed 3D-structures

High aspect ratio structures are promising for application in microbatteries with high energy and power density per footprint area. To investigate 3D-printed Si/C–graphite anodes with respect to their ARs, interdigitated structures were dispensed on copper substrates. Fig. 4 shows electron microscope images of printed 8-layer structures with slurries containing 12 wt%, 18 wt% and 24 wt% CMC/SBR binder. A structure with 6 wt% binder is not illustrated since the single fingers overlapped and could not be resolved (for 2 and 4 layers it was possible to print apparent interdigitated structures). This can be attributed to low values of the corresponding yield stress (see Fig. 3b and c). Obviously the AR value (apparent as "sharpness" in Fig. 4a–c) of the structure increases with increasing binder content.

Apart from that, all printed structures show strong adhesion to the copper substrate which is attributed to the adhesion properties of the CMC/SBR binder.[37] Fig. 5a shows the height and the width values of printed structures in dependence of the binder content and the number of layers. All values were determined at two positions (see Fig. 4c) using a confocal laser microscope. Regarding the height of the structures it can be seen, that the values increase with increasing binder content, which is consistent with the increased viscosity (in the low shear rate regime) and yield stress. As expected, height values of all samples containing ≥12 wt% binder increase linearly with similar slopes. The sample with 6 wt% binder suggests a steeper increase of height. However, two data points might be insufficient to make a reliable comparison. The linear increase of height values is in good accordance with literature values.[8,15,16] Additionally, Fu *et al.* presented values of *ca.* 1000 μm (height) at 6 layers which is very close to the data published here.[15]

In contrary, the width increases with decreasing binder content. It was suggested, that wider structures are due to a stronger melting tendency of the slurry. With respect to the rheological results it can be stated that higher rates of melting

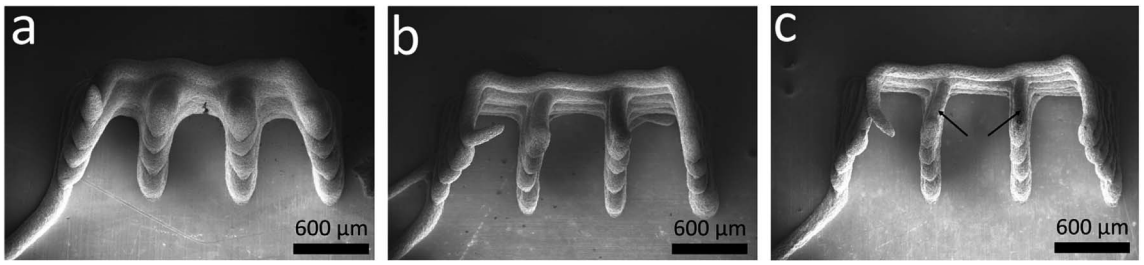

Fig. 4 Representative interdigitated Si/C–graphite blend anode structures containing (a) 12 wt%, (b) 18 wt% and (c) 24 wt% CMC/SBR binder printed on copper substrate. Values of height and width were measured at two positions of the structure, shown with arrows exemplary in (c).

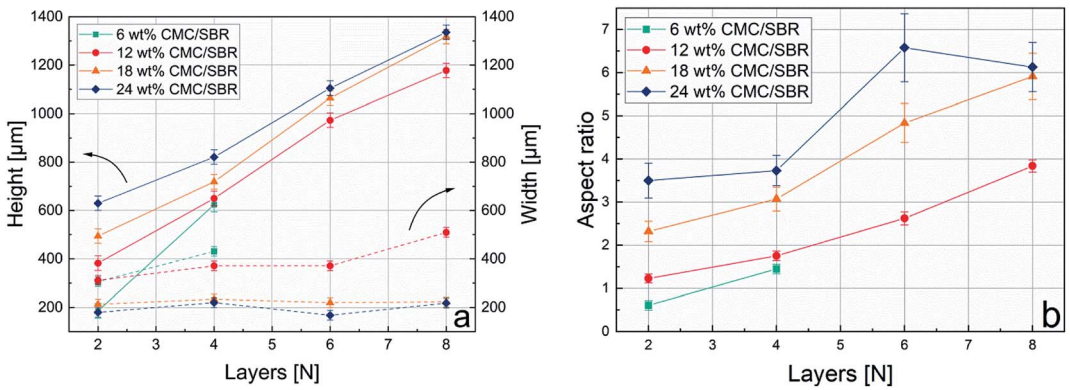

Fig. 5 (a) Selected height and width values of interdigitated printed anode structure with respect to printed layers and binder content. Values were determined by a scanning electron microscope. (b) Resulting AR values.

are related to decreased yield stress values and *vice versa*.[19,27] Interestingly samples with 18 wt% and 24 wt% binder show constant values at all number of layers. In contrast to that, samples with 6 wt% and 12 wt% binder show slightly increasing values which suggests melting due to lower yield stress. Similar behavior of high yield stress slurries is reported in literature.[8] Finally the resulting ARs are shown in Fig. 5b. In accordance with Fig. 5a ARs increase with increasing binder content and number of layers. It can be seen that the unsteady development of the AR values of the sample with 24 wt% binder is mainly due to minor fluctuations of the corresponding width. A printed 6-layer structure with 24 wt% binder shows the highest AR value of 6.5. The above presented dispensing results, *i.e.* height and width value evolution of the printed structures, are in accordance with rheological investigations, in particular with yield stress values. Here, it was confirmed that higher binder contents are necessary to get taller AR structures. Regarding the electrochemical characterization of the given anode structure with 18 wt% binder content the capacity per footprint area was calculated as 0.14 mA h mm^{-2}. For anode structures with binder content of 6, 12, 24 wt% the capacity per footprint area was not calculated since the corresponding anodes are not recommended for application in 3D-printed batteries and were thus not characterized in more detail.

Electrochemical performance

To investigate the electrochemical performance of the Si/C–graphite blend anodes for application in 3D-printed MLIBs cycling tests were performed using a standard coin cell setup. High capacity values at high current rates are crucial for MLIBs, thus rate capability tests can deliver the corresponding information. Fig. 6a shows capacity values depending on the binder content and C-rates. All blended anodes show increased charge capacity over the standard graphite anode whereas the anode with 12 wt% binder has the highest capacity increase by about 30% at C/2. Anodes with 12 wt% binder show stable cycling at C/4 with 484 mA h g^{-1} and capacity retention of 99.4% after 65 cycles. This result is in good agreement with recently published and industry-orientated silicon based anode materials.[38–40] With increasing C-rate the capacity of the cells decreases which is a well-known behavior and can be explained by kinetic limitations and pronounced ohmic drop behavior.[41] Interestingly, capacity values decrease with increasing binder content >12 wt%. Possible reasons for that are increased electrical resistance caused by the relatively huge amount of electrically insulating binder.[42] For a more detailed discussion regarding internal resistances of the anodes see ESI.†

Anodes with 6 wt% and 12 wt% binder at a current rate of 4C show high capacity retentions of 90% and 89% compared to cycling at C/4 which suggests lower internal resistance compared to anodes with higher binder content. Cell results are summarized for better comparison in Fig. 6b. The overall capacity retention after 65 cycles of all samples is close to 100%, which indicates minor irreversible capacity losses from fast charging. The sample with 6 wt% binder has the lowest capacity at C/4. Since the capacity drop with increasing C-rates is

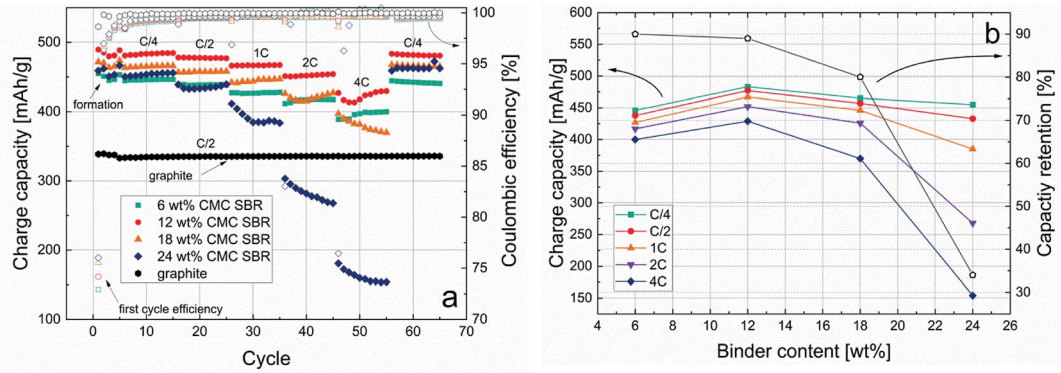

Fig. 6 (a) CCCV cycling of Si/C–graphite blend based lithium metal half cells in dependence of the binder content and the C-rate. (b) Charge capacity and capacity retention (between initial cycling at C/4 and 4C) in dependence of the binder content and C-rate.

comparable to the sample with 12 wt% binder the low capacity does likely not correspond to high internal resistance. A counteractive process might occur which leads to the low capacity values. A hypothesis could be low percolation of the anode and weak connectivity of active particles to the current collector.[18] It can be summarized that a Si/C–graphite blend slurry containing 12 wt% of CMC/SBR binder has the best performance regarding capacity and rate capability behavior. Based on this study a contrary development of electrochemical and rheological/printing properties could be found which indicates clearly that neither slurries with the lowest binder content (6 wt%) nor the highest (24 wt%) can be successfully applied in 3D-printed batteries. Thus, based on the given material formulation a slurry with 18 wt% binder content is recommended for 3D-printed IMLIBs since it combines high yield stress values (around 1500 Pa) and aspect ratios of close to 6 within an 8-layer structure with high capacity values (466 mA h g^{-1} at C/4) and considerable rate performance (around 427 mA h/g at 2C). To make lower binder content and higher capacity anodes suitable for 3D-printed IMLIBs, future study will focus on enhancing the printability of slurries by use of viscosity-increasing additives.

Conclusion

In this work we presented for the first time tailor-made Si/C composite blended graphite anode slurries for 3D-printed lithium ion microbatteries using a scalable dispensing process. Solvent and binder content were adapted to adjust the rheological properties regarding dispensing performance. Corresponding lithium metal cells with 12 wt% of binder were characterized by the best capacity and rate performance behavior using a coin cell setup. Although slurries had a relatively wide particle size distribution they could be successfully and reproducibly extruded through 110 μm commercially available micro nozzles without clogging. Rheological investigations, in particular the yield stress measurements, revealed that higher binder content for the dispensing process is favorable. In this regard 3D-printed interdigitated anode structures with 24 wt% binder showed high aspect ratios up to 6.5, which suggests them to be highly promising in fully printed 3D-IMLIBs. A fundamental trade-off between electrochemical and dispensing characteristics was found, whereby electrochemically optimized slurries lead to poor rheological and dispensing properties and *vice versa*. Thus, based on this study and the given material composition Si/C–graphite blend slurries with 18 wt% binder are recommended for application in 3D-IMLIB because it combines high capacity values (466 mA h g^{-1} at C/4) and considerable rate performance (around 427 mA h g^{-1} at 2C) with AR values close to 6 within an 8-layered structure. However, future work will focus on enabling the printability of lower binder content anodes with enhanced electrochemical performance by using viscosity-increasing additives. In summary, CMC/SBR is not only a suitable system for silicon based anodes from an electrochemical point of view but also because of the promoting ad- and cohesion properties in the dispenser printing process.

Conflicts of interest

The authors declare no competing financial interests.

Acknowledgements

The Baden-Wuerttemberg Stiftung is gratefully acknowledged for financing part of this work within the research project “ADD SPICE (IAF-04)”.

References

1 Y. Wang, B. Liu, Q. Li, *et al.*, Lithium and lithium ion batteries for applications in microelectronic devices: A review, *J. Power Sources*, 2015, **286**, 330–345.
2 M. Roberts, P. Johns, J. Owen, *et al.*, 3D lithium ion batteries—from fundamentals to fabrication, *J. Mater. Chem.*, 2011, **21**, 9876.
3 J. Bates, N. Dudney, B. Neudecker, *et al.*, Thin-film lithium and lithium-ion batteries, *Solid State Ionics*, 2000, **135**, 33–45.
4 P. Simon, Y. Gogotsi and B. Dunn, Where do batteries end and supercapacitors begin?, *Science*, 2014, **343**, 1210–1211.

5 B. E. Conway, *Electrochemical Supercapacitors: Scientific Fundamentals and Technological Applications*, Springer, 1999.
6 Q. Xia, S. Sun, J. Xu, *et al.*, Self-Standing 3D Cathodes for All-Solid-State Thin Film Lithium Batteries with Improved Interface Kinetics, *Small*, 2018, **14**, 1804149.
7 S. Sun, Q. Xia, J. Liu, *et al.*, Self-standing oxygen-deficient α-MoO_{3-x} nanoflake arrays as 3D cathode for advanced all-solid-state thin film lithium batteries, *Journal of Materiomics*, 2019, **5**, 229–236.
8 K. Sun, T.-S. Wei, B. Y. Ahn, *et al.*, 3D printing of interdigitated Li-ion microbattery architectures, *Adv. Mater.*, 2013, **25**, 4539–4543.
9 M. Singh, J. Kaiser and H. Hahn, Thick Electrodes for High Energy Lithium Ion Batteries, *J. Electrochem. Soc.*, 2015, **162**, A1196–A1201.
10 J. H. Pikul, H. Gang Zhang, J. Cho, *et al.*, High-power lithium ion microbatteries from interdigitated three-dimensional bicontinuous nanoporous electrodes, *Nat. Commun.*, 2013, **4**, 1732.
11 J. H. Pikul, J. Liu, P. V. Braun, *et al.*, Integration of high capacity materials into interdigitated mesostructured electrodes for high energy and high power density primary microbatteries, *J. Power Sources*, 2016, **315**, 308–315.
12 C. C. Ho, K. Murata, D. A. Steingart, *et al.*, A super ink jet printed zinc–silver 3D microbattery, *J. Micromech. Microeng.*, 2009, **19**, 94013.
13 K. Yoshima, H. Munakata and K. Kanamura, Fabrication of micro lithium-ion battery with 3D anode and 3D cathode by using polymer wall, *J. Power Sources*, 2012, **208**, 404–408.
14 T.-S. Wei, B. Y. Ahn, J. Grotto, *et al.*, 3D Printing of Customized Li-Ion Batteries with Thick Electrodes, *Adv. Mater.*, 2018, **30**, 1703027.
15 K. Fu, Y. Wang, C. Yan, *et al.*, Graphene Oxide-Based Electrode Inks for 3D-Printed Lithium-Ion Batteries, *Adv. Mater.*, 2016, **28**, 2587–2594.
16 D. Cao, Y. Xing, K. Tantratian, *et al.*, 3D Printed High-Performance Lithium Metal Microbatteries Enabled by Nanocellulose, *Adv. Mater.*, 2019, **31**, e1807313.
17 B. Berman, 3-D printing: The new industrial revolution, *Bus. Horiz.*, 2012, **55**, 155–162.
18 J. Li, X. Liang, F. Liou, *et al.*, Macro-/Micro-Controlled 3D Lithium-Ion Batteries via Additive Manufacturing and Electric Field Processing, *Sci. Rep.*, 2018, **8**, 1846.
19 M. Pospischil, *A Parallel Dispensing System for an improved Front Surface Metallization of Silicon Solar Cells*, Fraunhofer Verlag, 2017.
20 M. Pospischil, T. Riebe, A. Jimenez, *et al.*, Applications of parallel dispensing in PV metallization, *AIP Conf. Proc.*, **21561**, 20005.
21 *LS 13 320 Laser Diffraction Particle Size Analyzer: Instructions For Use*, https://www.beckmancoulter.com/wsrportal/techdocs?docname=B05577AB.pdf, accessed January, 2019.
22 I. Zimmermann, Möglichkeiten und Grenzen von Streulichtmeßverfahren, *Chem. Ing. Tech.*, 1996, **68**, 422–425.
23 S. Tepner, N. Wengenmeyr, L. Ney, *et al.*, Improving Wall Slip Behavior of Silver Pastes on Screen Emulsions for Fine Line Screen Printing, *Sol. Energy Mater. Sol. Cells*, 2019, **200**, 109969.
24 F. Clement, M. Linse, S. Tepner, *et al.*, "Project FINALE" – Screen and Screen Printing Process Development for Ultra-Fine-Line Contacts below 20μm Finger Width, *36th EU PVSEC Conference Proceedings*, 2019, pp. 259–262.
25 T. Mezger, *The rheology handbook: For users of rotational and oscillatory rheometers*, Vincentz Network, 2014.
26 M. Pospischil, M. Klawitter, M. Kuchler, *et al.*, Development of a high-throughput fine line metallization process using CFD-simulation'. *IEEE 39th Photovoltaic Specialists Conference (PVSC)*, 2013, pp. 2250–2253.
27 M. Pospischil, J. Specht, H. Gentischer, *et al.*, Correlations between Finger Geometry and Dispensing Paste Rheology, *27th European PV Solar Energy Conference and Exhibition*, 2012.
28 C. Meier, S. Lüttjohann, V. G. Kravets, *et al.*, Raman properties of silicon nanoparticles, *Phys. E*, 2006, **32**, 155–158.
29 J. Yu, J. Gao, F. Xue, *et al.*, Formation mechanism and optical characterization of polymorphic silicon nanostructures by DC arc-discharge, *RSC Adv.*, 2015, **5**, 68714–68721.
30 D. Shao, D. Tang, Y. Mai, *et al.*, Nanostructured silicon/porous carbon spherical composite as a high capacity anode for Li-ion batteries, *J. Mater. Chem. A*, 2013, **1**, 15068.
31 J. W. Ager III, D. K. Veirs, B. Marchon, *et al.*, Vibrational Raman characterization of hard-carbon and diamond films', *Optics, Electro-Optics, and Laser Applications in Science and Engineering*, 1991, pp. 24–31.
32 E. R. Buiel, A. E. George and J. R. Dahn, Model of micropore closure in hard carbon prepared from sucrose, *Carbon*, 1999, **37**, 1399–1407.
33 W. Xing, J. S. Xue and J. R. Dahn, Optimizing Pyrolysis of Sugar Carbons for Use as Anode Materials in Lithium-Ion Batteries, *J. Electrochem. Soc.*, 1996, **143**, 3046.
34 W. Mei, H. Chen, J. Sun, *et al.*, The effect of electrode design parameters on battery performance and optimization of electrode thickness based on the electrochemical–thermal coupling model, *Sustainable Energy Fuels*, 2019, **3**, 148–165.
35 G. Zhu, Y. Wang, S. Yang, *et al.*, Correlation between the physical parameters and the electrochemical performance of a silicon anode in lithium-ion batteries, *Journal of Materiomics*, 2019, **5**, 164–175.
36 M. Pospischil, M. Klawitter, M. Kuchler, *et al.*, High Speed Dispensing with Novel 6″ Print Head, *Energy Procedia*, 2016, **98**, 61–65.
37 D. Bresser, D. Buchholz, A. Moretti, *et al.*, Alternative binders for sustainable electrochemical energy storage – the transition to aqueous electrode processing and bio-derived polymers, *Energy Environ. Sci.*, 2018, **11**, 3096–3127.
38 S. Chae, N. Kim, J. Ma, *et al.*, One-to-One Comparison of Graphite-Blended Negative Electrodes Using Silicon Nanolayer-Embedded Graphite versus Commercial Benchmarking Materials for High-Energy Lithium-Ion Batteries, *Adv. Energy Mater.*, 2017, **7**, 1700071.
39 V. L. Chevrier, L. Liu, D. B. Le, *et al.*, Evaluating Si-Based Materials for Li-Ion Batteries in Commercially Relevant

Negative Electrodes, *J. Electrochem. Soc.*, 2014, **161**, A783–A791.

40 M. Marinaro, D.-h. Yoon, G. Gabrielli, *et al.*, High performance 1.2 Ah Si-alloy/Graphite|$LiNi_{0.5}Mn_{0.3}Co_{0.2}O_2$ prototype Li-ion battery, *J. Power Sources*, 2017, **357**, 188–197.

41 H. Buqa, D. Goers, M. Holzapfel, *et al.*, High Rate Capability of Graphite Negative Electrodes for Lithium-Ion Batteries, *J. Electrochem. Soc.*, 2005, **152**, A474.

42 N. Choi, Y. Lee and J. Park, Effect of cathode binder on electrochemical properties of lithium rechargeable polymer batteries, *J. Power Sources*, 2002, **112**, 61–66.

